






## Enzymatic upgrading of nanochitin using an ancient lytic polysaccharide monooxygenase

Leire Barandiaran<sup>1,4</sup>, Borja Alonso-Lerma<sup>1,4</sup>, Antonio Reifs<sup>1</sup>, Izaskun Larraza <sup>2</sup>, Raquel Olmos-Juste <sup>2</sup>, Alba Fernandez-Calvo<sup>1</sup>, Ylenia Jabalera <sup>1</sup>, Arantxa Eceiza <sup>2</sup> & Raul Perez-Jimenez <sup>1,3</sup>✉

Numerous enzymes have the potential to upgrade biomass, converting it into high-tech materials for new applications. However, the features of natural enzymes often limit their use beyond chemical conversion of the substrate. The development of strategies for the enzymatic conversion of biomass into high-value materials may broaden the range of applications of enzymes and enzyme design techniques. A relevant case is lytic polysaccharide monooxygenase (LPMO), a class of enzymes that catalyzes the oxidative cleavage of glycosidic bonds. Here, we show that an ancestral LPMO can generate chitin nanocrystals. Physicochemical characterization of the chitin nanocrystals demonstrates modifications that make it superior compared to chitin obtained by chemical treatments. We show that the nanocrystals are suitable for controlled 2D and 3D cell cultures, as well as for engineering a biomatrix that combines with graphene oxide, forming a hybrid conductive bioink.

<sup>1</sup>CIC nanoGUNE BRTA, Tolosa Hiribidea 76, 20018 San Sebastian, Spain. <sup>2</sup>Group 'Materials+Technologies', Department of Chemical and Environmental Engineering, Faculty of Engineering of Gipuzkoa, University of the Basque Country, Plaza Europa 1, 20018 San Sebastian, Spain. <sup>3</sup>Ikerbasque Foundation for Science, Plaza Euskadi 5, 48009 Bilbao, Spain. <sup>4</sup>These authors contributed equally: Leire Barandiaran, Borja Alonso-Lerma. ✉email: [r.perezjimenez@nanogune.eu](mailto:r.perezjimenez@nanogune.eu)

In the biotechnology industry, enzymes are the basis of complex substrate transformations into valuable chemicals for a myriad of applications, ranging from bioenergy to food industry<sup>1–5</sup>. Prominent examples are the enzymatic transformation, under specific conditions, of biomass into smaller molecules such as sugars, lignin, and chitosan<sup>6,7</sup>. Conversely, material science involves established chemical, physical and engineering procedures to transform and design novel materials, often by assembling small molecules used as building blocks<sup>8</sup>. Interestingly, multiple enzymes have the potential for upgrading and even creating novel high-tech functional materials<sup>9,10</sup>. However, this potential remains largely unexplored. Additionally, enzyme design and search techniques have not focused on optimizing the interaction of enzymes with materials for transforming them into a distinctive material with properties unattainable by conventional non-selective chemical and physical treatments. Therefore, searching for enzymes with the ability to upgrade rather than degrade materials stands up like a challenge for enzyme design techniques.

Cellulose and chitin are well suited for enzyme transformation into high-performance materials. They are highly abundant biopolymers in Nature. Cellulose is present in plants, while chitin is found in crustaceans, insects, and fungi. Both have been suggested as the source of valuable materials for numerous applications<sup>11–14</sup>. Numerous enzymes have been described to act on biomass including cellulases, laccases, chitinases, transglutaminases, transaminases, expansins, among others. These enzymes promote fiber disruption and chemical functionalization in a highly selective manner. Recently, a new class of oxidases was described, Lytic Polysaccharide Monooxygenase (LPMO), that are copper-associated metalloenzymes that catalyze the conversion of crystalline polysaccharides such as chitin and cellulose by oxidative cleavage of their  $\beta$ -(1  $\rightarrow$  4) glycosidic bond<sup>15,16</sup>, resulting in the selective oxidation of C1 and C4 carbons<sup>17,18</sup>. LPMOs expanded the toolbox of biomass-acting enzymes being one of the few enzymes that can actually modify biomass physically and chemically, i.e., by fiber disruption and chemical functionalization<sup>19</sup>.

Biomass is per se a recalcitrant material that often requires aggressive chemical treatments such as acid hydrolysis either with sulfuric acid or HCl, and these methods are considered less than ideal, especially for industrial settings. They require high temperature, and energy consumption, are environmentally hazardous, toxic, and require very expensive industrial settings. Looking for environmentally friendly solutions not only for

nanochitin, but for other biopolymers such as nanocellulose, is of special interest<sup>20,21</sup>. In recent decades, the improvement of biomass-acting enzymes has been object of intense research, but mainly focused on improving their efficiency to degrade biomass<sup>22</sup>. Recently, we designed an endonuclease enzyme that was not only capable of withstanding harsh conditions, but could also transform cellulose into high-performance crystalline nanocellulose, with features unattainable by other enzymes or acidic treatments<sup>23,24</sup>. Our endonuclease was designed using Ancestral Sequence Reconstruction (ASR)<sup>23</sup>. ASR has been traditionally used to trace the evolution of genes and proteins from extinct species to their modern descendant<sup>25–27</sup>, as well as to study ancient environmental conditions<sup>28,29</sup>. We and others realized that ancestral proteins displayed outstanding features such as elevated stability, efficiency, and chemical promiscuity that, although significant from an evolutionary point of view, could make enzymes potentially useful for biotechnology<sup>30–32</sup>. Other reports have also suggested the potential of ancestral enzymes as pharmaceuticals<sup>33</sup>. Today, we can consider ASR as a fine enzyme design technique that exploits the benefits of billions of years of molecular evolution on our planet.

In this work, we use ASR to design a new form of ancient LPMO. Using a vast collection of bacterial LPMOs, we reconstructed an LPMO sequence from a Firmicutes/Actinobacteria ancestor, the most ancient of our set of proteins (LFACA), about 3 billion years old. LFACA-LPMO displays typical traits of ancestral enzymes, such as high temperature and pH stabilities. Furthermore, LFACA-LPMO was able to degrade the complex structure of chitin (Fig. 1) into smaller fibers and nanofibers, much more efficiently than its modern counterpart from *Bacillus thuringiensis* (*Bt*LPMO). However, the most important feature of the new LPMO is that the enzymatic crystalline nanochitin produced (EnCNCh) showed physicochemical modifications that enhance its ability to serve as a stable functionalized biomaterial for cell growth in surfaces or solid three-dimensional matrixes, i.e., 2D and 3D cultures, respectively. Our results demonstrate that EnCNCh acts as versatile bioink that can also incorporate graphene derivatives. Given the growing importance of chitin in the biotechnology industry, EnCNCh emerges as a promising material for multiple applications<sup>11–13</sup>. This result again proves that ASR is a valuable technique capable of transforming enzymes into novel biocatalysts for upgrading biomass into high-performance materials.

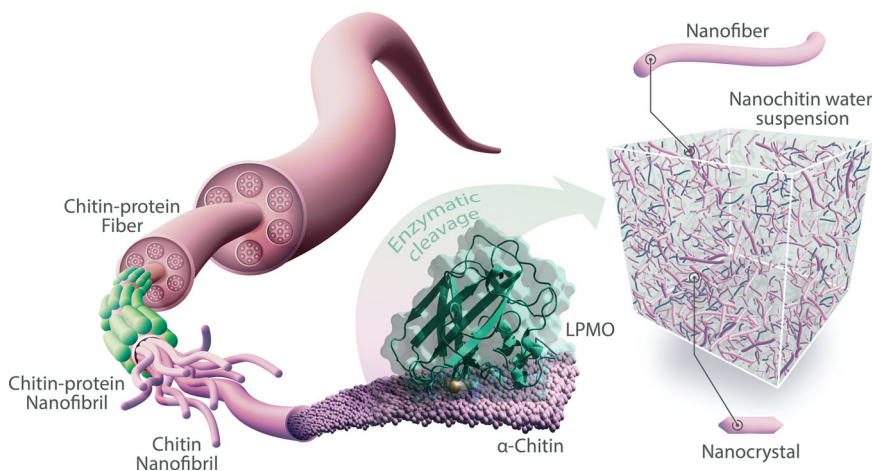


**Fig. 1 Illustration of  $\alpha$ -Chitin enzymatic oxidative cleavage.** The hierarchical structure of chitin allows deconstruction into nanoscale particles. To obtain chitin nanoparticles enzymatic oxidative cleavage was performed in natural  $\alpha$ -Chitin. Here, we represent how LPMO affinity to chitin fibers catalyses these fiber degradations into smaller fibers. Controlling cleavage time, we can obtain nanochitin with different sizes. Chitin nanocrystals (CNCh) are small crystalline particles with lengths between 100 and 500 nm and diameters between 3 and 40 nm.

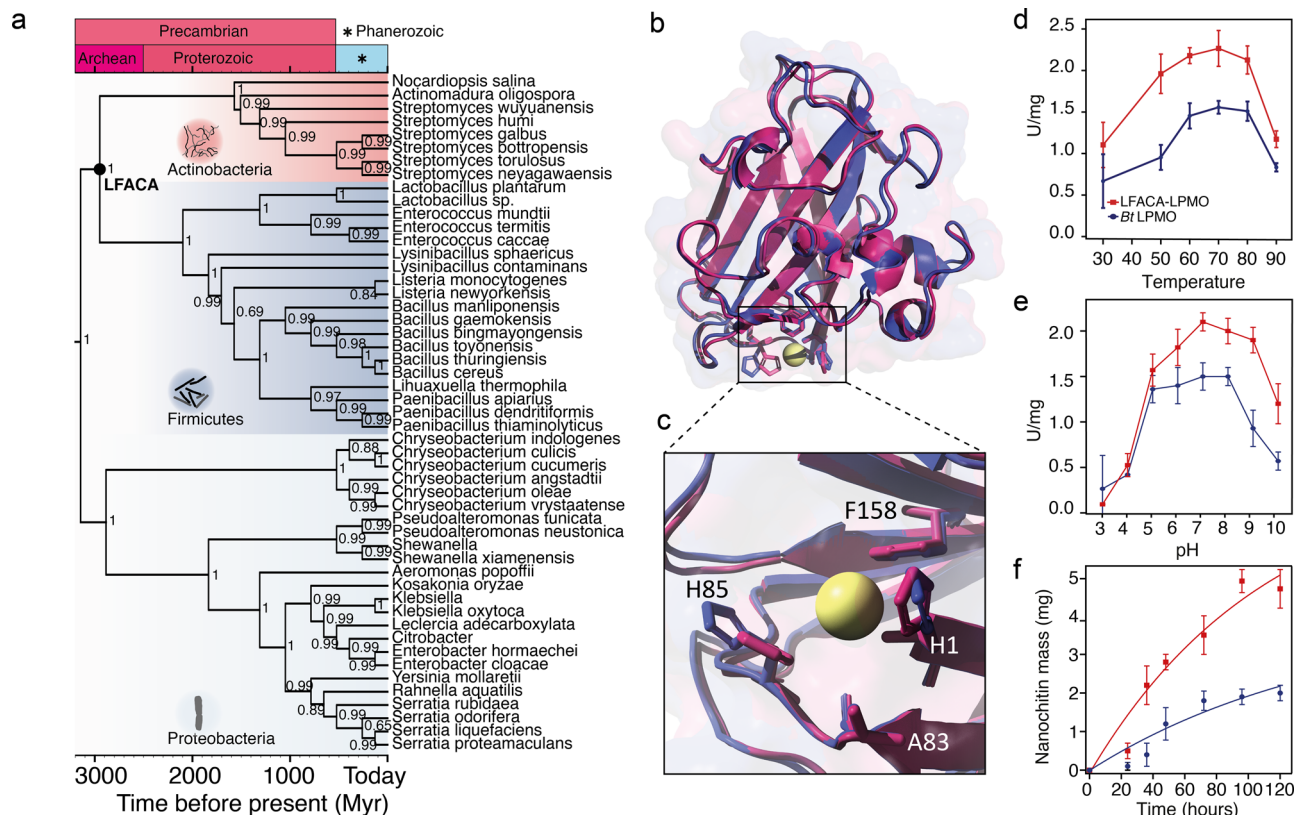


**Fig. 2 Ancestral LPMO reconstruction and characterization.** **a** Uncorrelated lognormal relaxed-clock chronogram of LPMO with geological time inferred with Bayesian inference. A total of fifty-one LPMO homologous sequences were used. Geological scale and times are indicated in the upper bar. The selected internal node for experimental validation is shown with a circle LFACA (Last Firmicutes Actinobacteria Common Ancestor). **b** LFACA-LPMO (red) and *Bt*LPMO (blue) AlphaFold2 prediction structure alignment with RMSD value of 0.428. **c** Active site Cu ion (yellow) and neighboring interacting residues at approximately 5 Å distance, conforming the so-called “histidine-brace”. **d** 2,6-DMP activity assay for LFACA-LPMO (red squares) and *Bt*LPMO (blue dots) at different temperatures, 30 °C to 90 °C. **e** pH activity assay from pH 3 to pH 10, LFACA-LPMO (red squares) and *Bt*LPMO (blue dots). For each data point, six independent experiments were collected. Data are shown as average  $\pm$  S.E.M. **f** Generation of nanochitin over time by oxidative cleavage of  $\alpha$ -Chitin by LFACA-LPMO (red squares) and extant *Bt*LPMO (blue dots). For each data point, three independent experiments were collected. Data are shown as average  $\pm$  S.D.

## Results

**Ancestral sequence reconstruction of ancient LPMO.** To infer the sequences of extinct bacterial LPMOs, we first retrieved from the UNIPROT database the sequence of fifty-one extant LPMOs from the AA10 family using as query sequence *Bt*LPMO (Supplementary Note 1), which has been described to act on chitin<sup>34</sup>. We obtained a diverse collection of sequences from Actinobacteria, Firmicutes, and Proteobacteria phyla, which diverged more than 3 Bya. This distribution indicates that LPMO were likely already present in organism that lived in the Archean eon. This is consistent with the idea of the ancient origin of chitinolytic enzymes in bacteria<sup>35</sup>. All fifty-one sequences were aligned, resulting in a compact and well-resolved alignment with significant conserved portions. Using the alignment, we obtained a phylogenetic chronogram using Bayesian inference<sup>36</sup>, in which the three clades were well resolved (Fig. 2a). The tree was dated using information from the Time Tree of Life (TTOL)<sup>37</sup>. Using both alignment and phylogeny, we inferred the most probable ancestral sequence for each node using maximum likelihood<sup>38,39</sup>, resulting posterior probabilities ranging from 0.87 to 0.99 (Supplementary Fig. 1). We selected for reconstruction the oldest node corresponding to the Last Firmicutes/Actinobacteria Common Ancestor (LFACA) of our collection, which lived  $\sim$ 3 Bya (Fig. 2a). LFACA-LPMO shares 63% identity with *Bt*LPMO.

We used the ancestral LPMO and the extant *Bt*LPMO sequences to predict their structure using the AlphaFold2 structure prediction

platform<sup>40,41</sup>. This software can infer structures with near-experimental accuracy. The platform offers prediction using five structural models. We chose the model with the highest confidence for structural comparison. Given that no x-Ray structure has been resolved for *Bt*LPMO, this analysis is a good first approximation for both proteins. Five structural models were predicted for each sequence and the model with the highest confidence was chosen for the structural analysis comparison. The estimated per-residue confidence score pLDDT (Local Difference Distance Test)<sup>42</sup>, is on average greater than 80 (Supplementary Fig. 2), with lower values at the termini, as expected. We performed a structural alignment with the inferred structures of both LPMOs yielding an RMSD value of 0.428 (Fig. 2b, c). We concentrated on the region where the functional copper cofactor is located. Residues H1 and F158, which are important in Cu interaction, align well with no displacement between the two enzymes. However, H85 seems to be displaced and the aromatic groups are positioned in different planes (Fig. 2b, c), which may affect Cu interaction. Other than that, no big structural differences are present between the two LPMOs despite the 40% difference in identity, including a conserved flat active site typical for AA10 family which may facilitate binding to crystalline chitin<sup>43</sup>. The gene encoding LFACA-LPMO was synthesized, cloned, and expressed in *E. coli* strains (Supplementary Fig. 3a). Ancestral LPMO express at higher levels than *Bt*LPMO, approximately 25% more (Supplementary Fig. 3b), a common feature of ancestral enzymes<sup>44</sup>.

**LPMO activity and EnCNCh obtention.** LPMO catalyzes the oxidative cleavage of carbohydrates such as cellulose and chitin. However, LPMO activity can be easily assayed by a colorimetric assay using 2,6-dimethoxyphenol (2,6-DMP) and  $\text{H}_2\text{O}_2$ <sup>45</sup> as substrate and co-substrate, respectively, releasing the product coerolignone, with stoichiometry 1:1. Following this test, we determined the activity of LFACA-LPMO in the temperature range 30–90 °C and compared it with the activity of *Bt*LPMO. As shown in Fig. 2d, LFACA-LPMO demonstrates higher activity at all temperatures, and the difference is especially significant in the 50–80 °C range with maximum performance at 70 °C for both. Similarly, the activity of LFACA-LPMO is higher than that of *Bt*LPMO in the pH range 4–10, especially above 5 (Fig. 2e). A higher thermal and pH performance is a common trait of ancestral enzymes<sup>31</sup>.

Given the ability of LPMO from family AA10 to cleave chitin, we tested the efficiency of LFACA-LPMO to generate nanochitin and compared it with extant *Bt*LPMO. We used as substrate  $\alpha$ -Chitin flakes without prior treatment, incubated with each LPMO enzyme and measured the mass of nanochitin produced at different times. As shown in Fig. 2f, nanochitin was obtained at much higher rate when using the ancestral LFACA-LPMO, i.e., 4 mg/72 h for LFACA-EnCNCh *versus* 1.8 mg/72 h for *Bt*EnCNCh. At seventy-two hours of reaction, we obtained the narrowest size distribution nanochitin fibers (Supplementary Fig. 4). The morphology of these nanochitin products was analyzed using atomic force microscopy (AFM) and compared with crystalline nanochitin obtained by acidic treatment (AcCNCh). As shown in Fig. 3a, CNCh is obtained after seventy-two hours reaction with both LPMOs. LFACA-EnCNCh shows an average length of 458 nm and diameter of 32.3 nm, while *Bt*EnCNCh features 502 nm in length and 35.5 nm in diameter (Fig. 3b). These proportions contrast with the size of AcCNCh, 178.6 nm of length and 15.0 nm and diameter (Fig. 3b and Supplementary Table 1). EnCNCh with both enzymes mainly shows fiber-like shapes preserving the natural and hierarchical structure of chitin, unlike acidic treatment that destroys amorphous parts without preserving its native structure<sup>46</sup>. Longer reaction times (96 h) seem to agglomerate CNCh through hydrogen bonds and Van der Waals forces, as previously reported for crystalline nanocellulose<sup>47</sup>.

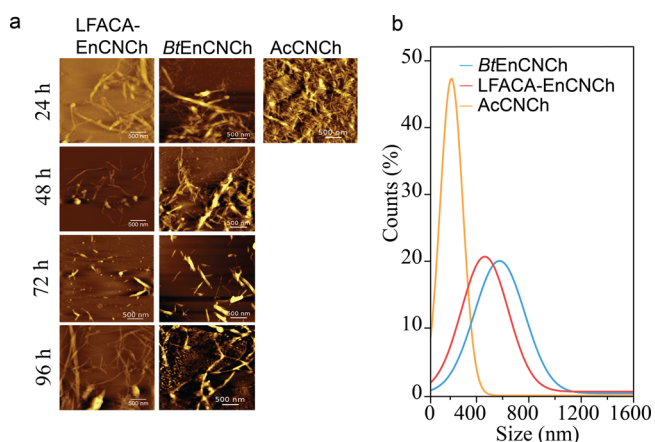


**Fig. 3 Nanochitin morphology.** **a** AFM images of nanoparticles produced by LPMO oxidative cleavage at different times. The images have  $3 \times 3 \mu\text{m}$  dimensions and show the nanoparticles obtained from the  $\alpha$ -Chitin cleavage with LFACA-LPMO and *Bt*LPMO at times of 24, 48, 72, and 96 h. **b** Size distribution of EnCNCh particles produced with LFACA-LPMO (red line), *Bt*LPMO (blue line) and HCl hydrolysis (yellow line) using  $\alpha$ -Chitin as substrate. Size distribution was calculated with the length of 100 particles from each condition.

To further analyze the chemical modifications made by enzymatic oxidative cleavage of LPMO in chitin, we used FTIR technique (Fig. 4a). FTIR spectra show all typical peaks of  $\alpha$ -chitin<sup>48,49</sup>. These peaks are in the region 2887–3440  $\text{cm}^{-1}$ . We also observe peaks at 1654 and 1621  $\text{cm}^{-1}$  (amide I) attributed to  $\alpha$ -chitin, peak at 1555  $\text{cm}^{-1}$  (amide II), peaks at 1379 and 1314  $\text{cm}^{-1}$  (C–H stretching of methyl groups), 1260  $\text{cm}^{-1}$  (amide III), peaks at 1010–1070  $\text{cm}^{-1}$  (carbohydrate backbone) and peak at 898  $\text{cm}^{-1}$  (glycopyranose bond). The oxidative cleavage of LPMO after 72 h reaction can be observed by the appearance of small bands in the region of 1740  $\text{cm}^{-1}$ , which is consistent with the reported band for protonated carboxyl groups observed in TEMPO oxidation of  $\alpha$  and  $\beta$ -chitin<sup>49–53</sup>, and even LPMO-treated cellulose<sup>54</sup>. We estimated the  $A_{1740}/A_{1030}$  ratio, related to carboxylate groups content<sup>50</sup>, for both LFACA-EnCNCh and *Bt*EnCNCh, with values of 0.05 and 0.02, respectively, thus indicating higher oxidation for LFACA-EnCNCh. Also, an increased intensity of the peak at 1621  $\text{cm}^{-1}$  is observed<sup>49</sup>, (Fig. 4b, Supplementary Figs. 5 and 6).

Furthermore, chemical analysis by  $^{13}\text{C}$  CP/MAS NMR showed that EnCNCh maintained native chitin structure. Additionally, oxidation is demonstrated by a shoulder at 178 ppm from carboxyl groups<sup>55</sup> (inset in Fig. 4c). Another new chemical signature in EnCNCh is demonstrated by a peak at 30 ppm in the CP/MAS  $^{13}\text{C}$  NMR spectra (Fig. 4c) that we believe to be a methyl group oxidized to  $\text{CH}_2\text{O}^-$ . TEMPO-oxidized chitin or chitin nanocrystals do not show this peak<sup>56</sup>, suggesting that LPMO-mediated oxidation is different than that of TEMPO oxidation. In addition, thermogravimetric analysis shows an effect on thermal stability by LPMO oxidative cleavage; EnCNCh showed a degradation temperature of 374 °C which is slightly lower than that of recalcitrant  $\alpha$ -chitin at 394 °C and AcCNCh at 385 °C (Fig. 4d and Supplementary Table 2). As expected, the introduction of carboxyl groups modifies the thermal stability<sup>49</sup>. Finally, using XRD analysis, we see the regular peaks of  $\alpha$ -chitin at 9.3°, 19.1°, 20.6°, 23.2°, and 26.2°, which correspond to (020), (110), (120), (130) and (013) planes<sup>57</sup>, respectively (Fig. 4e). EnCNCh maintains native crystal structure with a crystallinity index (CI) of approximately 85%, very similar to that of  $\alpha$ -chitin (Fig. 4e and Supplementary Table 3). Within the experimental error, no remarkable variation in crystallite size is observed, which has also been observed in other oxidative processes<sup>53</sup>. We also measured zeta ( $\zeta$ ) potential of the LPMO-EnCNCh and  $\alpha$ -chitin, resulting in 31.3 and 39.4 mV, respectively. This decrease in the case of LPMO-EnCNCh may be attributed to the highest content of carboxyl groups due to oxidation.

Overall, these results demonstrate that LPMO, whether ancestral or modern, can produce EnCNCh with physical characteristics similar to native chitin, but chemically modified by adding carboxyl group that could serve as functional groups. However, what makes LFACA-LPMO special is its ability to efficiently produce EnCNCh, with the potential to be used as a distinct high-tech biomaterial.

### Nanomaterial fabrication and 3D printing with EnCNCh.

EnCNCh maintain native chitin features but also incorporates chemical modifications such as carboxyl groups. The superior efficiency of LFACA-LPMO to produce EnCNCh brings the possibility of applying this new form of chitin for further applications. We wanted to test if the different properties found in EnCNCh versus AcCNCh would allow better performance in bioprinting. This would be interesting to use nanochitin as a novel material for tissue engineering. In fact, chitosan obtained from chitin is already in use for this type of application. However, chitosan is often mixed with other components, such as collagen, to generate a stable matrix for bioprinting<sup>58</sup>. Therefore, the possibility of

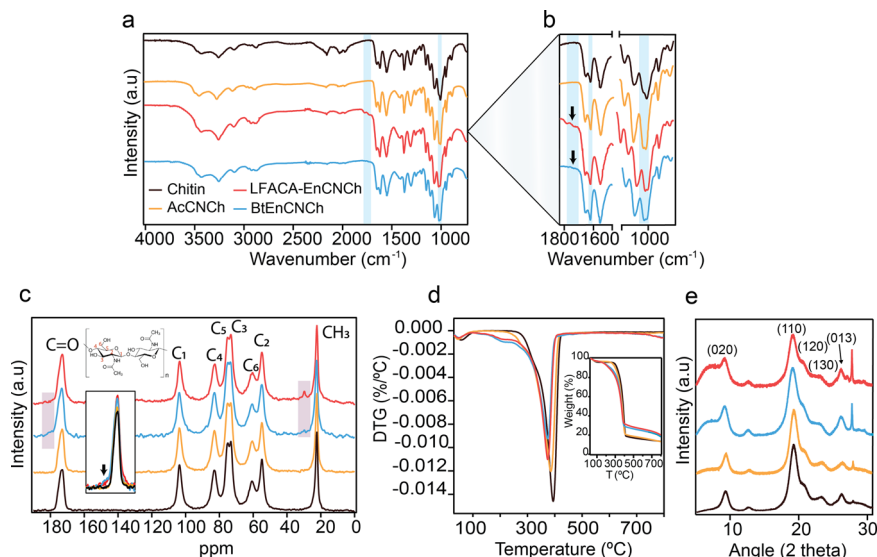


**Fig. 4 Nanochitin physicochemical characterization.** **a** FTIR spectra of  $\alpha$ -chitin (black line), CNCh produced by oxidative cleavage of  $\alpha$ -Chitin with LFACA-LPMO (LFACA-EnCNCh, red line), BtLPMO (BtEnCNCh, blue line) and hydrochloric acid (AcCNCh, yellow line). Spectra from 4000 to 750  $\text{cm}^{-1}$ . **b** details of the significant incipient peaks of CNCh at 1740  $\text{cm}^{-1}$ , 1621  $\text{cm}^{-1}$ , and 1030  $\text{cm}^{-1}$ . **c** CP/MAS  $^{13}\text{C}$  NMR spectra of  $\alpha$ -chitin (black line), LFACA-EnCNCh (red line) produced with LFACA-LPMO enzymatic oxidative cleavage, BtEnCNCh (blue line) produced with extant BtLPMO oxidative cleavage and AcCNCh (yellow line) produced by hydrochloric acid hydrolysis. Inset in the region 178 ppm. **d** Thermogravimetric analysis curves of  $\alpha$ -Chitin (black line), LFACA-EnCNCh (red line) produced with LFACA-LPMO enzymatic oxidative cleavage, BtEnCNCh (blue line) produced with BtLPMO enzymatic oxidative cleavage and AcCNCh (yellow line) produced by hydrochloric acid hydrolysis. Inset of weight loss curves and derivative from TGA curves. **e** XRD diffractogram for crystalline  $\alpha$ -chitin (black line), LFACA-EnCNCh (red line), BtEnCNCh (blue line), AcCNCh (yellow line).

having a single-component matrix for bioprinting makes EnCNCh potentially better than chitosan. To test the ability of EnCNCh obtained with LFACA-LPMO for bioprinting, we concentrated a suspension to 10% EnCNCh and loaded it into a syringe extruder on a 3D printer (Fig. 5a). The printed pieces maintain the shape of the programmed scaffold. Conversely, CNCh obtained with chemical treatment was unable to form such stable scaffolds. We seeded HEK293T cells on the EnCNCh scaffold and allows then to proliferate for three days. Cells were dyed with DAPI and CellOrange to observe both the nucleus and cytoplasm of living cells that migrated and proliferated within the EnCNCh matrix (Fig. 5b, c). Similarly, we tested whether EnCNCh could be assembled as a stable 2D substrate for surface cell growth. We prepared EnCNCh films (Fig. 5d) that were stable immersed in water (Supplementary Fig. 7) and cell culture media. HEK293T-cells adhered well to the EnCNCh substrate and were able to proliferate (Fig. 5e, f). Interestingly, EnCNCh did not support *Staphylococcus aureus* attachment (Fig. 5g, h), which is in line with the antibacterial activity reported for chitin and chitosan<sup>59</sup>.

The above experiments demonstrate that EnCNCh is a distinct material resulting from the physicochemical conversion of chitin by LFACA-LPMO, which can serve as a matrix and substrate for cell proliferation. We also wondered if EnCNCh could be mixed with other materials to create functional nanobiocomposites that potentiate the physical, chemical, and biological characteristics of EnCNCh. Nanomaterials with controlled electrical properties are being investigated<sup>60</sup>, and a key aspect sought is their biocompatibility for biomedical applications<sup>61</sup>. We reasoned that a nanocomposite containing EnCNCh and graphene oxide would fulfill these requirements, i.e., it would be able to form stable, printable, conductive and biocompatible films.

We prepared EnCNCh hybrid films containing graphene oxide (GO) in different proportions from 0.3 to 15 wt% (Fig. 6a and Supplementary Fig. 8). GO mixed well with EnCNCh and chemically reduced after film assembly (rGO). Using SEM, we analyzed the morphology and chemical composition of the reduced

films demonstrating the dispersion of rGO in the EnCNCh matrix (Supplementary Fig. 9). We also analyzed chemical composition by FTIR (Supplementary Fig. 10), and no chemical changes were observed in chitin as % rGO increased. We measured the conductivity of our reduced films observing and increasing conductivity with rGO content (Supplementary Table 4). The conductivity reached a plateau of 11.1 S/m at approximately 10 wt% rGO content. With these measurements we determined the electrical percolation threshold ( $\rho_c$ ) following the percolation theory<sup>62</sup>. We plotted the conductivity against the volumetric rGO content (Fig. 6b) and calculated a  $\rho_c$  of 0.10% for EnCNCh. This value in our system corresponds to 0.25 wt% rGO, which is in the range determined for other graphene nanocomposites<sup>63</sup>. AcCNCh could not form stable films with rGO as they dispersed in water during the reduction step. This hybrid material could perfectly be used as conductive ink for printing (Fig. 6c). To the best of our knowledge, this is the first time that CNCh has been used to create hybrid nanocomposites with graphene that show printing and conductive capabilities.

As mentioned above, we envision these films as the basis for obtaining printable conductive bioinks. We prepared a mixture of EnCNCh 10 wt% suspension and added 5 wt% GO and used it for printing. The printed ink was then freeze dried and the scaffold was further reduced. We seeded HEK293T cells onto the 3D printed scaffolds to test the viability of the hybrid material (Fig. 6d). After three days of culture, we dyed cells with DAPI and CellOrange dyes to observe both the nucleus and cytoplasm using fluorescence microscopy (Fig. 6e). We also tested the ability of EnCNCh/rGO films for 2D cell growing and proliferation by seeding films with the HEK293T cells (Supplementary Fig. 11). Altogether, we observed that HEK293T cells adhere and proliferate well in our artificial substrate.

## Discussion

Protein design techniques have provided superb examples of improved enzymes for biotechnological applications<sup>64</sup>. But the

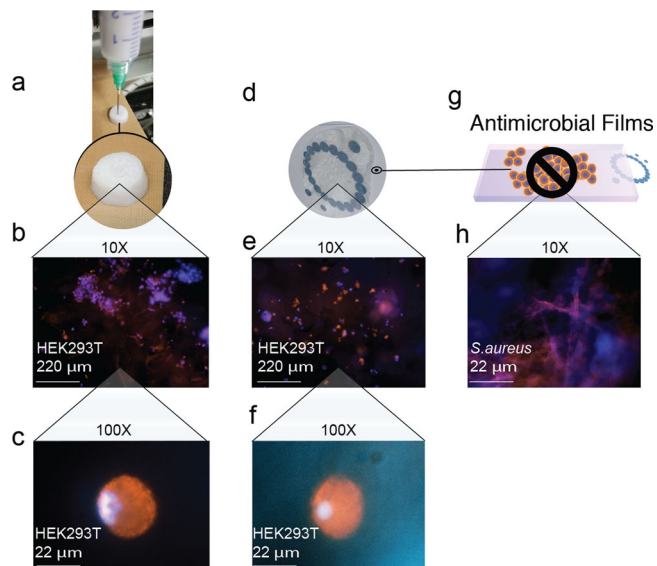


**Fig. 5 Cell culture on EnCNCh.** **a** Image of LFACA-EnCNCh cylindrical scaffold 3D printing, where HEK293T cells were seeded. **b** Confocal microscopy image at 10X and **(c)** 100X of HEK293T-stained nuclei with DAPI and cell membrane with Orange Plasma. Cells proliferated embedded on EnCNCh matrix after 3 days of culture. **d** Picture of EnCNCh film where HEK293T cells were grown. **e** Confocal microscopy image at 10X and **(f)** 100X of HEK293T stained with DAPI and Orange Plasma seeded and grown on the film. **g** Representation of EnCNCh film where *S. aureus* bacteria do not grow after 24 h of incubation. **h** Confocal images of EnCNCh film after incubating *S. aureus*.

vast majority of them are intended to enhance one specific feature needed for an already known application<sup>65</sup>. In the case of biomass transformation, most modifications are directed toward improving the degrading capability of enzymes under certain working conditions<sup>66</sup>. Conversely, other protein design techniques have been developed to generate enzymes with functions that do not exist in natural proteomes<sup>67,68</sup>. However, quite often these techniques are aimed at transforming or generating small molecules as chemical products. Not many examples exist on enzyme improvements for the use of enzymes in material engineering, most specifically for the generation of novel biomaterials. For the most part, enzymes have been viewed as biomolecules useful in a biochemical context largely unrelated to any material engineering technique. Here, we report how an enzyme design technique based on the principles of evolution, i.e., ancestral sequence reconstruction, can be used to generate an ancestral LPMO enzyme. The ancestral LPMO produces nanochitin at a rate 2.5 folds higher than the extant counterpart, with a 50% increase in efficiency at a broad range of temperature and pH, and with a 25% increase in production yield. Achieving these improvements in a single round of protein design is extremely challenging with any other protein design technique. This new enzyme can be considered a novel synthetic biocatalyst capable of transforming chitin into nanosized chitin crystals, EnCNCh. Although production of nanosized particles by LPMOs have been shown before<sup>54,69</sup>, here we present a bottom-up approach that starts with the design of a new LPMO that is used to build a novel material and probing its potential applications.

The new EnCNCh is chemically and physically modified in a single-transformation reaction and can be used as a single-component matrix for 2D and 3D cell cultures. EnCNCh accepts well a graphene derivative, making it a good candidate for inkjet-printing conductive inks that also allow the attachment of living cells. Thus, our results are important from a biochemical point of view, as they bring a totally new enzyme with biochemical

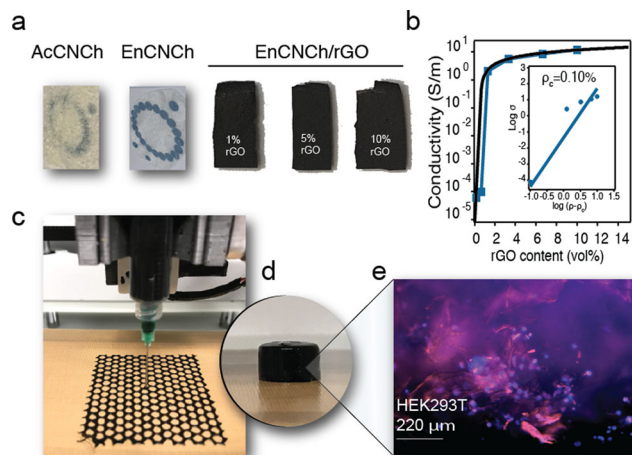


**Fig. 6 EnCNCh/rGO films fabrication.** **a** Detail of CNCh films from left to right: AcCNCh film, EnCNCh film (obtained with LFACA-LPMO), EnCNCh film 1%wt rGO, 5%wt rGO and 10 wt rGO. EnCNCh is transparent and had good integrity unlike AcCNCh that was very weak and not as translucent. **b** Conductivity of EnCNCh for different reduced graphene contents: 0.3, 1, 2, 5, 10 and 15 wt% rGO (blue squares and blue line to guide the eye) and fitting (black line). Calculations were made with volumetric % of reduced graphene oxide. In the inset, a log-log plot for the determination of electrical percolation threshold of the material ( $P_c$ ) (blue dots and fitting with blue line). **c** Image of 3D EnCNCh + 5% GO 3D printing of a stable honeycomb-like scaffold. **d** Picture of a EnCNCh + 5% GO 3D printed bottom shape scaffold where HEK293 cells were grown. **e** Confocal microscopy image at X10 of HEK293T-stained nuclei with DAPI and Orange Plasma seeded and grown on the hybrid material.

capabilities nonobvious to any existing LPMO; but we also generate a new upgraded form of chitin unattainable by any known procedure. We have previously shown very similar features for an ancestral endoglucanase enzyme that acting on cellulose was able to generate high-performance crystalline nanocellulose, EnCNC<sup>23,24</sup>. We hypothesize that these materials alone or in combination can offer potential benefits in a myriad of applications, representing a new class of enzymatic biomaterials.

Our results pave the way towards new research in material science, bringing enzyme catalysis into the toolbox of physicochemical transformations in materials. As in the case of nanocellulose, EnCNCh is especially attractive for applications in biomedicine such as tissue engineering and bioprinting. However, we believe that the significance of our results has a much broader perspective and represents a novel advance in material science. The properties of our modified enzymes allow controlling the physicochemical features of the most abundant polymers on Earth, which permits the generation of new high-tech materials from renewable bioresources. We believe that this could be extended to many other enzymes and proteins that act on biopolymers, realizing the benefits of using natural resources both from a technological and environmental point of view. Finally, we would like to remark that the entire bioengineering process reinforces the need for a global collaborative scientific framework that connects many scientific disciplines and take advantage of collective knowledge.

## Methods

**Ancestral sequence reconstruction (ASR) of LPMO.** Fifty-one LPMO from auxiliary activity family 10 (AA10) were downloaded from the NCBI database. Sequences belong to three bacterial phyla: Proteobacteria, Actinobacteria, and Firmicutes. All sequence ID numbers are listed in Supplementary Note 1. The alignment of the sequences was performed using MUSCLE extension on the

MEGA platform<sup>70</sup>. We inferred the best evolutionary model using MEGA, resulting in the Jones-Taylor-Thornton (JTT) with gamma distribution model. The phylogeny was carried out using BEAST v1.10.4 package software, including the BEAGLE library for parallel processing and Bayesian inference using Markov chain Monte Carlo (MCMC). Phyla were well separated with no further action; however, we established monophyletic groups for Proteobacteria, Actinobacteria, and Firmicutes to set priors. We set JTT model with eight gamma categories and invariant distributions, Yule model for speciation, 20 million generations of length chain, and sampling every 1000 generations. The divergence times were estimated by uncorrelated log-normal clock model (UCLN), using molecular information from Time Tree Of Life (TTOL) with default birth and death rates<sup>37</sup>. Calculations were run in a multicore server. From the generated trees we discarded the 25% of them as burn-in with the LogCombiner utility from BEAST. We verified the MCMC log file using TRACER and ensured all parameters showed effective sample size (ESS) > 100. Posterior probabilities of all nodes were above 0.65, and most of them were near 1. Figtree software v1.4.2 was used to visualize and edit the phylogenetic tree. Finally, ancestral sequence reconstruction was performed by maximum likelihood using PAML 4.8 with a gamma distribution for variable replacement rates across sites and the JTT model<sup>71</sup>. Posterior probabilities were calculated for all amino acids, and the residue with the highest posterior probability was chosen for each site. High posterior probabilities ensure the correctness of each bifurcation given the sequence collection, alignment and model used. We selected Last Actinobacteria/Firmicutes common ancestor (LAFCA) for laboratory resurrection.

**Structure prediction using AlphaFold2.** The AlphaFold2 models<sup>40,42</sup> were calculated using the ColabFold platform<sup>72</sup>. We used query sequences in Supplementary Note 2 as input. We use fast MMseqs2 homology search to build a multiple sequence alignment using default parameters. Model with higher average pLDDT was chosen for comparison of each predicted structure. Visualization of the resulting models was performed with PyMol (The PyMOL Molecular Graphics System, Version 2.0 Schrödinger, LLC.).

**Protein expression and purification.** We used the previously described protocol for LPMO expression and purification<sup>73</sup>. Genes encoding the ancestral and extant LPMO proteins were synthesized, and codon optimized for expression in *E. coli* cells (Life Technologies). A native signal peptide was included to secure export to the periplasmic space (Supplementary Note 2). This translocation ensures cleavage of the signal peptide leaving a histidine at the N-terminus, essential for copper cofactor binding<sup>74</sup>. The genes were cloned into pQE-80L vector and transformed onto *E. coli* BL21 cells (DE3) (Life Technologies) for protein expression<sup>75</sup>. Bacteria were incubated in LB medium at 37 °C until OD<sub>600</sub> reached 0.6; IPTG was added to the medium to 1 mM concentration for protein induction overnight at 20 °C. Bacterial cultures were collected by centrifugation for 10 min at 4000G and 4 °C, and periplasmic extraction was performed by osmotic shock method. Pellets were resuspended in 30 mL of spheroplast buffer (1 M Tris-HCl pH 7.5, 0.5 M sucrose, 0.5 mM EDTA). Resuspended pellets were incubated on ice and then centrifuge for 10 min at 5000G and 4 °C. The supernatants were discarded and incubated for 10 min at room temperature, followed by resuspension on 25 mL ice-cold water. After 45 s of the resuspension step, we added 1.25 mL of cold 20 mM MgCl<sub>2</sub>. The mixture was then centrifuged at 15,000G for 10 min at 4 °C. We collected the supernatant and filter it (0.22 μm pore size). The supernatants were copper saturated by incubation with Cu(II)SO<sub>4</sub> at a ratio of 1:3 for 30 min at room temperature<sup>76</sup>. The proteins were then further purified, and the non-bonded copper was removed by size exclusion chromatography using a Superdex 200HR column (GE Healthcare). The buffer used was 50 mM sodium phosphate pH 7.0. The purified proteins were finally verified by SDS-PAGE with 12% acrylamide gels. The protein concentration was calculated by measuring the absorbance at 280 nm in Nanodrop 2000C, using the equation  $280 \text{ of } \times \text{M}^{-1} \text{cm}^{-1}$  and MW of  $\times \text{g mol}^{-1}$ , with the theoretical extinction coefficient of  $\epsilon_{280} = 39,545 \text{ M}^{-1} \text{cm}^{-1}$  and molecular mass of 20 kDa without signal peptide.

**LPMO characterization.** Reactions were performed in 96-well plates mixing 166 μL of 100 mM phosphate buffer pH 8, 20 μL of 10 mM DMP (final concentration of 1 mM), 38 and 4 μL of 5 mM H<sub>2</sub>O<sub>2</sub> (final concentration of 0.1 mM). Finally, we added 10 μL of enzyme dilution at a suitable concentration to each well in a final volume of 200 μL per well. Plates were orbitally mixed, and the reaction was carried out at 50 °C. Activity was calculated by measuring the increase of absorbance at 469 nm for 5 min using the molar absorption coefficient of coeruleinone ( $\epsilon_{469} = 53,200 \text{ M}^{-1} \text{cm}^{-1}$ ) to calculate the peroxidase activity of LPMO. For thermal stability assay, we preincubated the LPMO enzymes to the test temperatures for 5 min in a 1.5 mL Eppendorf tube in a thermo mixer and then placed them on ice for 5 min. The reaction was carried out at a 96-well plate at 50 °C, 169.5 μL 100 mM phosphate buffer pH 8, 20 μL 10 mM DMP as a chromogenic substrate to a final concentration of 1 mM, 0.5 μL of 5 mM H<sub>2</sub>O<sub>2</sub>, and 10 μL of enzyme dissolution with adequate enzyme concentration to a final volume of 200 μL. Absorbance at 469 nm was measured for 30 min at Epoch 2 spectrophotometer. For pH assay, different pH buffer dissolutions were prepared from pH

3 to pH 10: 100 mM citric acid for pH 3–5, 100 mM phosphate buffer for pH 6–7, 100 mM carbonate buffer for pH 8 and 100 mM Boric acid for 9–10.

**Nanochitin enzymatic isolation and characterization.** Commercial α-Chitin from Sigma Aldrich was used as substrate. We used 2.5% α-Chitin suspension in water with a ratio of 10 mg of each enzyme (LFACA-LPMO and BtLPMO) per gram of substrate. As reducing agent, we used 2 mM ascorbic acid from Sigma Aldrich. The oxidative cleavage was carried out at 50 °C in agitation for 72 h. Reactions were stopped by placing them on ice, and the mixtures were sonicated with a microtip sonicator UPH 100H Ultrasonic Processor (Hielscher) for 25 min at 75% to separate aggregated nanoentities. Nanochitin was isolated by several centrifugation steps and concentrated by ultracentrifugation at 33,000 G for 30 min. Pellets were resuspended in water or 2% acetic acid and lyophilized in a Telstar Lyoquest for physical and chemical characterization by freeze-drying for 24 h. Nanochitin produced by hydrochloric acid form was donated from “Material and Technology group (GMT)” from UPV/EHU.

**Fourier transform infrared (FTIR).** The infrared spectra were recorded in attenuated reflection (ATR) mode to analyze functional groups of lyophilized samples of chitin, EnCNCh, and acid CNCh. We used a Perkin-Elmer Frontier FTIR spectrophotometer equipped with an ATR sampling stage within the wavenumber of 4000 and 650 cm<sup>-1</sup>, with 32 scans and a resolution of 4 cm<sup>-1</sup>.

**Atomic force microscopy (AFM).** We used a Nanoscope V scanning probe microscope (Multimode 8 Bruker Digital instruments) using an integrated force generated by cantilever/silicon probes. Images were obtained at room temperature, in taping mode, applying 320 kHz resonance frequency and 5–10 nm tip radius and 125 μm long. Sample preparation was made by spin coating using a Spincoater P6700 at 200 rpm for 60 s on mica substrate. AFM height and phase images were collected simultaneously in all the samples. The size of the images was 3 × 3 μm, and nanofibers of different sizes were distinguished. The length and diameter of 100 nanofibers was measured to calculate the average length, diameter, and aspect ratio (Length/Diameter).

**X-ray diffraction (XRD).** Crystalline structure, crystallinity, and crystallite size of nanochitin was studied using X-ray diffraction (XRD) powder diffraction patterns. Data were collected at room temperature using a Philips X'pert PRO automatic diffractometer from 5 to 50 ° and a PIXcel solid-state detector (active length in 2θ 3.347°) operating at 40 kV and 40 mA, in theta configuration, a secondary monochromator with Cu-Kα radiation (λ = 1.5418 Å) and a PIXcel solid-state detector (active length in 2θ 3.347°). We used an antiscattering slit and a fixed divergence giving a constant volume of sample illumination. From the normalized and deconvoluted diffractograms, the crystallinity index (CI%) was calculated by Segal equation<sup>77</sup> (1):

$$\text{Crystallinity index(\%)} = (I_{110} - I_{am})/I_{110} \times 100 \quad (1)$$

where  $I_{110}$  is the intensity of the chitin crystalline peak and  $I_{am}$  is the intensity of the amorphous peak. Crystallite size was measured using Scherrer's Eq. (2):

$$\beta = \kappa\lambda/\tau \cos \theta \times 100 \quad (2)$$

where λ is the wavelength of the incident X-ray, θ is the angle of the (110) plane, “β” is the full width at half maximum of the (110) peak, τ is the crystallite size, and κ is a constant value.

**<sup>13</sup>C CP/MAS NMR analysis.** We used solid-state cross-polarization magic angle spinning <sup>13</sup>C nuclear magnetic resonance (<sup>13</sup>C CP/MAS NMR). <sup>13</sup>C CP/MAS NMR spectra were measured using a 400 MHz BRUKER system equipped with a 4 mm MASDVT TRIPLE Resonance HYX MAS probe. 2K scans were taken at Larmor frequencies of 400.17 MHz and 100.63 MHz for <sup>1</sup>H and <sup>13</sup>C nuclei. Chemical shifts were reported relative to the signals of <sup>13</sup>C nuclei in glycine. The sample rotation frequency was 12 kHz, and relaxation delay was 5 s. Polarization transfer was achieved with RAMP cross-polarization (ramp on the proton channel) with a contact time of 5 ms. High-power SPINAL 64 heteronuclear proton decoupling was applied during acquisition.

**Thermogravimetric analysis.** TGA was used to study the thermal stability of nanochitin and hybrid nanopapers. The data was recorded using TGA/SDTA 851 Mettler Toledo equipment, where 10 mg of the samples were heated from 30 to 800 °C in a nitrogen atmosphere with a scanning rate of 10 °C/min. The initial degradation temperature ( $T_d$ ) is described as the loss of 5% of the weight of the total sample and the maximum degradation temperature ( $T_d$ ) is the minimum of the degradation peak in the derivative of the thermogravimetric curves (DTG).

Zeta potential (ζ, mV) of LPMO-EnCNCh and α-chitin were measured using a Zetasizer Ultra (Malvern Instrument) at 25 °C. Nanocrystals were suspended in deionized water at final concentration of 0.1 wt% and homogenized by sonication.

**Nanochitin EnCNCh/graphene films and bioinks.** Nanochitin films were prepared by casting method with an EnCNCh suspension of 1 wt% sonicated for 1 h. The suspension was placed in a Teflon mold and dried for 2 h at 50 °C. Conductive films were fabricated by EnCNCh suspension and with graphene oxide (GO) at different final concentrations: 0.3, 1, 2, 5, 10, and 15% wt of GO. GO (4 wt% water suspension) was kindly supplied by Graphenea (San Sebastian, Spain). The mixture was sonicated in a bath to assure homogeneity and cast with the help of a vacuum bomb using an Ultrafiltration disc of 30 KDa from Merck. The wet film was dried at 50 °C for 2 h, obtaining films with a thickness of approximately 50 µm. GO in the nanopapers was reduced by placing the films in ascorbic acid solution (30 mg/mL) for 2 h at 95 °C and then washed using milliQ water before drying the films at 50 °C for 2 h.

Bioinks for 3D printing were prepared with 10 %wt EnCNCh suspension and 5 %wt graphene oxide. The mixture was sonicated in a bath to ensure homogeneity. After printing and freeze-drying the scaffolds, GO in the scaffold was reduced by placing the films in ascorbic acid solution (30 mg/mL) for 2 h at 95 °C and then washed using milliQ water before drying the films at 50 °C for 2 h.

**Scanning electrical microscopy.** The morphology of the nanopaper surface and graphene was analyzed by SEM using a FEI ESEM Quanta 200 microscope operating at 5–20 kV. Nanopapers were put on carbon tape for adhesion.

Electrical conductivity was measured by a four-point probe method using a Probe Station 4 Everbeig. The specific resistances ( $q$ ) were calculated with the sheet resistances ( $R_s$ , Ω/squares) and the thickness of the nanopapers ( $t$ , cm) in Eq. (3):

$$q = R_s \times t \quad (3)$$

We used the specific resistance calculated to infer the corresponded conductivity (S/cm) with the following Eq. (4) that was transformed to S/m.

$$r = 1/q \quad (4)$$

The percolation threshold,  $\rho_c$ , was measured using a power-law Eq. (5) based on the percolation theory:<sup>60</sup>

$$\sigma = \sigma_f \times (\rho - \rho_c)^n \quad (5)$$

where  $\sigma$  is the conductivity of the nanopaper,  $\rho_f$  is the rGO conductivity,  $\rho$  is the rGO content expressed at volume fraction, and  $n$  is the exponent describing the rapid variation of the conductivity near the percolation threshold ( $\rho_c$ ).

**3D printing of EnCNCh-based scaffold.** Scaffolds were printed using a Voladora 3D printer (Tumaker, S.L. Spain) which has been modified for layer-by-layer syringe extrusion 3D printing. Honeycomb-like scaffold and button-like scaffolds were printed directly on poly- tetrafluoroethylene slides at room temperature using a needle of 0.8 mm in diameter and speed of 5 mm/s.

**2D and 3D cell cultures.** HEK293T was maintained in DMEN + 10% FBS medium supplemented with 1% (w/v) L-glutamine and penicillin–streptomycin (100 IU/ml). Before growing cells in our material, EnCNCh film and EnCNCh scaffold were sterilized by UV for 3 h. 20,000 cells were seeded on each substrate and let to growth for 3 days in the incubator at 37 °C in 5% CO<sub>2</sub>. Cells were fixed in 4% formaldehyde for 30 min and washed with PBS. Films were dehydrated by increasing concentration of ethanol solution until 100% concentration of ethanol was reached. After fixation, cells were dyed with DAPI solution (5 mg/ml), and CellMask Orange Plasma membrane Stain (5 mg/mL) diluted in PBS (1:2000) and after washing each sample three times with PBS. DAPI-Orange Plasma-stained cells were observed after 20 min of incubation by confocal microscopy.

## Data availability

Data supporting the findings of this study are available from the corresponding author upon reasonable request.

Received: 5 March 2022; Accepted: 1 August 2022;

Published online: 15 August 2022

## References

- Lin, N. & Dufresne, A. Surface chemistry, morphological analysis and properties of cellulose nanocrystals with gradiented sulfation degrees. *Nanoscale* **6**, 5384–5393 (2014).
- Liao, J. C., Mi, L., Pontrelli, S. & Luo, S. Fuelling the future: microbial engineering for the production of sustainable biofuels. *Nature Rev. Microbiol.* **14**, 288–304 (2016).
- Rasor, J. P. & Voss, E. Enzyme-catalyzed processes in pharmaceutical industry. *Appl. Catal. A: Gen.* **221**, 145–158 (2001).
- Vemula, P. K., Li, J. & John, G. Enzyme catalysis: tool to make and break amygdalin hydrogelators from renewable resources: a delivery model for hydrophobic drugs. *J. Am. Chem. Soc.* **128**, 8932–8938 (2006).
- Zhang, Y., Geary, T. & Simpson, B. K. Genetically modified food enzymes: a review. *Curr. Opin. Food Sci.* **25**, 14–18 (2019).
- Kaczmarek, M. B., Struszczyk-Swita, K., Li, X., Szczesna-Antczak, M. & Daroch, M. Enzymatic modifications of chitin, chitosan, and chitoooligosaccharides. *Front. Bioeng. Biotechnol.* **7**, 243 (2019).
- You, C. et al. Enzymatic transformation of nonfood biomass to starch. *Proc. Natl Acad. Sci.* **110**, 7182–7187 (2013).
- Gaspar, V. M., Lavrador, P., Borges, J., Oliveira, M. B. & Mano, J. F. Advanced bottom-up engineering of living architectures. *Adv. Mater.* **32**, 1903975 (2020).
- Richter, M., Schulenburg, C., Jankowska, D., Heck, T. & Faccio, G. Novel materials through Nature's catalysts. *Mater. Today* **18**, 459–467 (2015).
- Peschke, T. et al. Self-assembling all-enzyme hydrogels for flow biocatalysis. *Angew. Chem. Int. Ed. Engl.* **57**, 17028–17032 (2018).
- Jayakumar, R., Menon, D., Manzoor, K., Nair, S. V. & Tamura, H. Biomedical applications of chitin and chitosan based nanomaterials—a short review. *Carbohydrate Polym.* **82**, 227–232 (2010).
- Zhang, Y. et al. Preparation, assessment, and comparison of α-chitin nano-fiber films with different surface charges. *Nanoscale Res. Lett.* **10**, 1–11 (2015).
- Uddin, A. J., Fujie, M., Sembo, S. & Gotoh, Y. Outstanding reinforcing effect of highly oriented chitin whiskers in PVA nanocomposites. *Carbohydrate Polym.* **87**, 799–805 (2012).
- Kontturi, E. & Spirk, S. Ultrathin films of cellulose: a materials perspective. *Front. Chem.* **7**, 488 (2019).
- Vaaje-Kolstad, G. et al. An oxidative enzyme boosting the enzymatic conversion of recalcitrant polysaccharides. *Science* **330**, 219–222 (2010).
- Agger, J. W. et al. Discovery of LPMO activity on hemicelluloses shows the importance of oxidative processes in plant cell wall degradation. *Proce. Natl Acad. Sci.* **111**, 6287–6292 (2014).
- Beeson, W. T., Phillips, C. M., Cate, J. H. & Marletta, M. A. Oxidative cleavage of cellulose by fungal copper-dependent polysaccharide monoxygenases. *J. Am. Chem. Soc.* **134**, 890–892 (2012).
- Horn, S. J., Vaaje-Kolstad, G., Westereng, B. & Eijsink, V. Novel enzymes for the degradation of cellulose. *Biotechnol. Biofuels* **5**, 45 (2012).
- Villares, A. et al. Lytic polysaccharide monoxygenases disrupt the cellulose fibers structure. *Sci. Rep.* **7**, 1–9 (2017).
- Fernández-Marín, R. et al. Eco-friendly isolation and characterization of nanochitin from different origins by microwave irradiation: Optimization using response surface methodology. *Int. J. Biol. Macromol.* **186**, 218–226 (2021).
- Muñoz-Núñez, C., Fernández-García, M. & Muñoz-Bonilla, A. Chitin nanocrystals: environmentally friendly materials for the development of bioactive films. *Coatings* **12**, 144 (2022).
- Banerjee, G., Scott-Craig, J. S. & Walton, J. D. Improving enzymes for biomass conversion: a basic research perspective. *BioEnergy Res.* **3**, 82–92 (2010).
- Alonso-Lerma, B. et al. High performance crystalline nanocellulose using an ancestral endoglucanase. *Commun. Mater.* **1**, 1–10 (2020).
- Alonso-Lerma, B. et al. Enzymatically produced cellulose nanocrystals as reinforcement for waterborne polyurethane and its applications. *Carbohydrate Polym.* **254**, 117478 (2021).
- Manteca, A. et al. Mechanochemical evolution of the giant muscle protein titin as inferred from resurrected proteins. *Nat. Struct. Mol. Biol.* **24**, 652–657 (2017).
- Perez-Jimenez, R. et al. Single-molecule paleoenzymology probes the chemistry of resurrected enzymes. *Nat. Struct. Mol. Biol.* **18**, 592–596 (2011).
- Nakano, S., Niwa, M., Asano, Y. & Ito, S. Following the evolutionary track of a highly specific L-arginine oxidase by reconstruction and biochemical analysis of ancestral and native enzymes. *Appl. Environ. Microbiol.* **85** (2019).
- Gaucher, E. A., Govindarajan, S. & Ganesh, O. K. Palaeotemperature trend for Precambrian life inferred from resurrected proteins. *Nature* **451**, 704–707 (2008).
- García, A. K., Schopf, J. W., Yokobori, S.-I., Akanuma, S. & Yamagishi, A. Reconstructed ancestral enzymes suggest long-term cooling of Earth's photic zone since the Archean. *Proc. Natl Acad. Sci.* **114**, 4619–4624 (2017).
- Gumulya, Y. et al. Engineering highly functional thermostable proteins using ancestral sequence reconstruction. *Nat. Catal.* **1**, 878–888 (2018).
- Barruetabeña, N. et al. Resurrection of efficient Precambrian endoglucanases for lignocellulosic biomass hydrolysis. *Commun. Chem.* **2**, 1–13 (2019).
- Thomas, A., Cutlan, R., Finnigan, W., van der Giezen, M. & Harmer, N. Highly thermostable carboxylic acid reductases generated by ancestral sequence reconstruction. *Commun. Biol.* **2**, 429 (2019).
- Zakas, P. M. et al. Enhancing the pharmaceutical properties of protein drugs by ancestral sequence reconstruction. *Nat. Biotechnol.* **35**, 35–37 (2017).



34. Zhang, H., Zhao, Y., Cao, H., Mou, G., & Yin, H. Expression and characterization of a lytic polysaccharide monoxygenase from *Bacillus thuringiensis*. *Int. J. Biol. Macromol.* **79**, 72–75 (2015).
35. Lacombe-Harvey, M.-É., Brzezinski, R. & Beaulieu, C. Chitinolytic functions in actinobacteria: ecology, enzymes, and evolution. *Appl. Microbiol. Biotechnol.* **102**, 7219–7230 (2018).
36. Randall, R. N., Radford, C. E., Roof, K. A., Natarajan, D. K. & Gaucher, E. A. An experimental phylogeny to benchmark ancestral sequence reconstruction. *Nat. Commun.* **7**, 1–6 (2016).
37. Hedges, S. B., Marin, J., Suleski, M., Paymer, M. & Kumar, S. Tree of life reveals clock-like speciation and diversification. *Mol. Biol. Evol.* **32**, 835–845 (2015).
38. Drummond, A. J., Suchard, M. A., Xie, D. & Rambaut, A. Bayesian phylogenetics with BEAUti and the BEAST 1.7. *Mol. Biol. Evol.* **29**, 1969–1973 (2012).
39. Xu, B. & Yang, Z. PAMLX: a graphical user interface for PAML. *Mol. Biol. Evol.* **30**, 2723–2724 (2013).
40. Jumper, J. et al. Highly accurate protein structure prediction with AlphaFold. *Nature* **596**, 583–589 (2021).
41. Tunyasuvunakool, K. et al. Highly accurate protein structure prediction for the human proteome. *Nature* **596**, 590–596 (2021).
42. Varadi, M. et al. AlphaFold Protein Structure Database: massively expanding the structural coverage of protein-sequence space with high-accuracy models. *Nucleic Acids Res.* **50**, D439–D444 (2021).
43. Forsberg, Z. et al. Comparative study of two chitin-active and two cellulose-active AA10-type lytic polysaccharide monoxygenases. *Biochemistry* **53**, 1647–1656 (2014).
44. Hendrikse, N. M., Charpentier, G., Nordling, E. & Syrén, P. O. Ancestral diterpene cyclases show increased thermostability and substrate acceptance. *FEBS J.* **285**, 4660–4673 (2018).
45. Breslmayr, E. et al. A fast and sensitive activity assay for lytic polysaccharide monoxygenase. *Biotechnol. Biofuels* **11**, 1–13 (2018).
46. Goodrich, J. D. & Winter, W. T.  $\alpha$ -Chitin nanocrystals prepared from shrimp shells and their specific surface area measurement. *Biomacromolecules* **8**, 252–257 (2007).
47. Araki, J., Yamanaka, Y. & Ohkawa, K. Chitin-chitosan nanocomposite gels: reinforcement of chitosan hydrogels with rod-like chitin nanowhiskers. *Polym. J.* **44**, 713–717 (2012).
48. Shankar, S., Reddy, J. P., Rhim, J.-W. & Kim, H.-Y. Preparation, characterization, and antimicrobial activity of chitin nanofibrils reinforced carrageenan nanocomposite films. *Carbohydrate Polym.* **117**, 468–475 (2015).
49. Oun, A. A. & Rhim, J.-W. Effect of oxidized chitin nanocrystals isolated by ammonium persulfate method on the properties of carboxymethyl cellulose-based films. *Carbohydrate Polym.* **175**, 712–720 (2017).
50. Chen, R., Huang, W.-C., Wang, W. & Mao, X. Characterization of TEMPO-oxidized chitin nanofibers with various oxidation times and its application as an enzyme immobilization support. *Marine Life Sci. Technol.* **3**, 85–93 (2020).
51. Fan, Y., Saito, T. & Isogai, A. Chitin nanocrystals prepared by TEMPO-mediated oxidation of  $\alpha$ -chitin. *Biomacromolecules* **9**, 192–198 (2008).
52. Fan, Y., Saito, T. & Isogai, A. TEMPO-mediated oxidation of  $\beta$ -chitin to prepare individual nanofibrils. *Carbohydrate Polym.* **77**, 832–838 (2009).
53. Jiang, J. et al. Chitin nanocrystals prepared by oxidation of  $\alpha$ -chitin using the O<sub>2</sub>/laccase/TEMPO system. *Carbohydrate Polym.* **189**, 178–183 (2018).
54. Koskela, S. et al. Lytic polysaccharide monoxygenase (LPMO) mediated production of ultra-fine cellulose nanofibres from delignified softwood fibres. *Green Chem.* **21**, 5924–5933 (2019).
55. El Hariri El Nokab, M. & van der Wel, P. C. A. Use of solid-state NMR spectroscopy for investigating polysaccharide-based hydrogels: a review. *Carbohydrate Polym.* **240**, 116276 (2020).
56. Kato, Y., Kaminaga, J., Matsuo, R. & Isogai, A. TEMPO-mediated oxidation of chitin, regenerated chitin and N-acetylated chitosan. *Carbohydrate Polym.* **58**, 421–426 (2004).
57. Pereira, A. G. B., Muniz, E. C. & Hsieh, Y.-L. 1H NMR and 1H–13C HSQC surface characterization of chitosan–chitin sheath-core nanowhiskers. *Carbohydrate Polym.* **123**, 46–52 (2015).
58. Ma, L. et al. Collagen/chitosan porous scaffolds with improved biostability for skin tissue engineering. *Biomaterials* **24**, 4833–4841 (2003).
59. Kucharska, M., Sikora, M., Brzoza-Malczewska, K. & Owczarek, M. In *Chitin Chitosan: Properties and Applications* (eds. Van den Broek, L. A. M. & Boeriu, C. G.) 169–187 (Wiley, 2019).
60. Zhu, C., Monti, S. & Mathew, A. P. Cellulose nanofiber–graphene oxide biohybrids: disclosing the self-assembly and copper-ion adsorption using advanced microscopy and ReaxFF simulations. *ACS nano* **12**, 7028–7038 (2018).
61. Huang, Q. & Zhu, Y. Printing conductive nanomaterials for flexible and stretchable electronics: a review of materials, processes, and applications. *Adv. Mater. Technol.* **4**, 1800546 (2019).
62. Kirkpatrick, S. Percolation and conduction. *Rev. Mod. Phys.* **45**, 574 (1973).
63. Marsden, A. et al. Electrical percolation in graphene–polymer composites. *2D Materials* **5**, 032003 (2018).
64. Li, C., Zhang, R., Wang, J., Wilson, L. M. & Yan, Y. Protein engineering for improving and diversifying natural product biosynthesis. *Trends Biotechnol.* (2020).
65. Woodley, J. M. Protein engineering of enzymes for process applications. *Curr. Opin. Chem. Biol.* **17**, 310–316 (2013).
66. Østby, H., Hansen, L. D., Horn, S. J., Eijssink, V. G. H. & Várnai, A. Enzymatic processing of lignocellulosic biomass: principles, recent advances and perspectives. *J. Ind. Microbiol. Biotechnol.* **47**, 623–657 (2020).
67. Basanta, B. et al. An enumerative algorithm for de novo design of proteins with diverse pocket structures. *Proc. Natl Acad. Sci.* **117**, 22135–22145 (2020).
68. Grayson, K. J. & Anderson, J. L. R. Designed for life: biocompatible de novo designed proteins and components. *J. R. Soc. Interface* **15**, 20180472 (2018).
69. Wang, D. et al. Production of functionalised chitins assisted by fungal lytic polysaccharide monoxygenase. *Green Chem.* **20**, 2091–2100 (2018).
70. Manuel, M. A new semi-subterranean diving beetle of the *Hydroporus* normandi-complex from south-eastern France, with notes on other taxa of the complex (Coleoptera: Dytiscidae). *Zootaxa* **3652**, 453–474 (2013).
71. Yang, Z. PAML 4: phylogenetic analysis by maximum likelihood. *Mol. Biol. Evol.* **24**, 1586–1591 (2007).
72. Mirdita, M. et al. ColabFold—Making protein folding accessible to all. *bioRxiv* <https://doi.org/10.1101/2021.08.15.456425> (2021).
73. Courtade, G., Le, S. B., Saetrom, G. I., Brautaset, T. & Aachmann, F. L. A novel expression system for lytic polysaccharide monoxygenases. *Carbohydrate Res.* **448**, 212–219 (2017).
74. Gaber, Y. et al. Heterologous expression of lytic polysaccharide monoxygenases (LPMOs). A mini-review. *Biotechnol. Adv.* **43**, 107583 (2020).
75. Kim, E. Y., Jakobson, C. M. & Tullman-Ereck, D. Engineering transcriptional regulation to control Pdu microcompartment formation. *PLoS ONE* **9**, e113814 (2014).
76. Stepanov, A. A. et al. Unraveling the roles of the reductant and free copper ions in LPMO kinetics. *Biotechnol. Biofuels* **14**, 28 (2021).
77. Segal, L., Creely, J., Martin, A. Jr & Conrad, C. An empirical method for estimating the degree of crystallinity of native cellulose using the X-ray diffractometer. *Textile Res. J.* **29**, 786–794 (1959).

## Acknowledgements

This work has been supported by grants PID2019-109087RB-I00 to R.P.-J. from Spanish Ministry of Science and Innovation. This project has received funding from the European Union's Horizon 2020 research and innovation program under grant agreement No 964764 to R.P.-J. 'Materials + Technologies' Research Group also acknowledges UPV/EHU and the Basque Government in the frame of "Research Group" (GIU 18/216) and "Grupos Consolidados" (IT776-13), respectively. We also thank Gipuzkoako Foru Aldundia for financial Support. HEK293T cells were a kind gift from Dr. Maria Muñoz Caffarel (Biodonostia, San Sebastian, Spain).

## Author contributions

R.P.-J. conceived the project. R.P.-J. and A. E. designed research. L. B., B. A.-L., A. R., I.L., R.O.-J., A. F.-C., Y.J., carried out all experimental measurements and preparations including protein and sample preparation, activity assays, and instrumental measurements. L.B., B. A.-L., A. E., and R. P.-J. performed data analysis. A. E. and R. P.-J. wrote the manuscript and all authors contributed to revising and editing the manuscript.

## Competing interests

The authors declare no Competing Financial Interests but the following Competing Non-Financial Interests: R. P.-J., L.B. and B. A.-L. are co-inventors on patent application filed by CIC nanoGUNE, "Novel Lytic Polysaccharide Monoxygenase and uses thereof". European Patent Application P21139EP00. All other authors have no competing interests to declare.

## Additional information

**Supplementary information** The online version contains supplementary material available at <https://doi.org/10.1038/s43246-022-00277-9>.

**Correspondence** and requests for materials should be addressed to Raul Perez-Jimenez.

**Peer review information** *Communications Materials* thanks the anonymous reviewers for their contribution to the peer review of this work. Primary Handling Editor: John Plummer. Peer reviewer reports are available.

**Reprints and permission information** is available at <http://www.nature.com/reprints>

**Publisher's note** Springer Nature remains neutral with regard to jurisdictional claims in published maps and institutional affiliations.



**Open Access** This article is licensed under a Creative Commons Attribution 4.0 International License, which permits use, sharing, adaptation, distribution and reproduction in any medium or format, as long as you give appropriate credit to the original author(s) and the source, provide a link to the Creative Commons license, and indicate if changes were made. The images or other third party material in this article are included in the article's Creative Commons license, unless indicated otherwise in a credit line to the material. If material is not included in the article's Creative Commons license and your intended use is not permitted by statutory regulation or exceeds the permitted use, you will need to obtain permission directly from the copyright holder. To view a copy of this license, visit <http://creativecommons.org/licenses/by/4.0/>.

© The Author(s) 2022